

ARTICLE OPEN



Switchable half-metallicity in A-type antiferromagnetic NiI₂ bilayer coupled with ferroelectric In₂Se₃

Yaping Wang¹, Xinguang Xu¹, Xian Zhao², Weixiao Ji³, Qiang Cao³, Shengshi Li³✉ and Yanlu Li¹✉

Electrically controlled half-metallicity in antiferromagnets is of great significance for both fundamental research and practical application. Here, by constructing van der Waals heterostructures composed of two-dimensional (2D) A-type antiferromagnetic NiI₂ bilayer (bi-NiI₂) and ferroelectric In₂Se₃ with different thickness, we propose that the half-metallicity is realizable and switchable in the bi-NiI₂ proximate to In₂Se₃ bilayer (bi-In₂Se₃). The polarization flipping of the bi-In₂Se₃ successfully drives transition between half-metal and semiconductor for the bi-NiI₂. This intriguing phenomenon is attributed to the joint effect of polarization field-induced energy band shift and interfacial charge transfer. Besides, the easy magnetization axis of the bi-NiI₂ is also dependent on the polarization direction of the bi-In₂Se₃. The half-metallicity and magnetic anisotropy energy of the bi-NiI₂ in heterostructure can be effectively manipulated by strain. These findings provide not only a feasible strategy to achieve and control half-metallicity in 2D antiferromagnets, but also a promising candidate to design advanced nanodevices.

npj Computational Materials (2022)8:218; <https://doi.org/10.1038/s41524-022-00904-6>

INTRODUCTION

Antiferromagnetic (AFM) spintronics^{1–3}, as a frontier area of research, is expected to bring about the revolutionary progress for the next-generation spintronic devices. This is because the antiferromagnets possess various fascinating features, such as robustness against external magnetic field perturbation, absence of parasitic stray field, and ultrafast dynamics^{4–7}. To utilize AFM materials as the active elements in spintronics, several key issues remain to be resolved, in which the generation and manipulation of half-metallicity or fully spin polarized current are very important aspects⁸. Achieving the half-metallicity through the electric field has been pursued recently⁹, due to the superiority of low power and fast response, and it is conducive to the implementation of fully electrical reading/writing¹⁰. Recently, the long sought electric field controlled half-metallicity was predicted in two-dimensional (2D) A-type AFM VSe₂ bilayer which features with intralayer ferromagnetic (FM) and interlayer AFM couplings¹¹. However, the achieved half-metallicity is volatile since the fully spin polarized conduction electron would dissipate with the removal of the electric field, which is less desirable for memory and logic devices. As a result, it is urgently required a practical scheme for a nonvolatile electrical controlled half-metallicity.

Recently, van der Waals (vdW) heterostructure has attracted extensive attention for both fundamental science and technological application^{12–14}, which offers a platform to realize intriguing physics and functionalities by flexibly stacking layered material with various properties. One of the most representative examples is the multiferroic vdW heterostructure constructed based on 2D FM and ferroelectric (FE) materials, which shows a strong interfacial magnetoelectric effect, such as FE controlled half-metallicity and magnetic order^{15–20}. The FE layer, on the one hand, is to provide a spontaneous polarization field, which enables the control of the electronic or magnetic properties of FM layer. On the other hand, the FE layer holds different work functions at two surfaces, which diversifies the interfacial charge transfer with the reversal of the electric polarization, providing an effective avenue

for band structure engineering. Motivated by such a principle, here we propose that the half-metallicity in 2D A-type antiferromagnet can be achieved by introducing a FE substrate with out-of-plane electric polarization to construct a multiferroic heterostructure. Figure 1a presents a schematic illustration of spin- and layer-projected density of state (DOS) for an A-type AFM bilayer. Although there is no spin polarization in the total DOS, the inherent ferromagnetism of monolayer makes the different spin subbands locate on different monolayer spatially. Such a characteristic provides an opportunity to realize the half-metallicity by breaking the inversion symmetry. When the 2D A-type antiferromagnet is deposited on a FE substrate, shown in Fig. 1b, the presence of the polarization field and possible interfacial charge transfer due to work function difference are expected to trigger the different electrostatic potential between two FM layers. In this context, the DOS associated with layer-1 will be shifted downwards with respect to that of layer-2. The ultimate result of this phenomenon is likely to lead to a metallic band with single spin polarization at the Fermi level (E_F), as depicted in Fig. 1c, and thus the half-metallicity emerges. Furthermore, it is possible to switch the half-metallicity by reversing the FE polarization of the substrate.

Hitherto, tremendous progress in the preparation of vdW magnetic materials has provided an opportunity for exploring and utilizing the 2D A-type AFM materials^{21–24}. Very recently, the NiI₂ bilayer (bi-NiI₂) has been successfully fabricated on the h-BN substrate, which was predicted as an A-type AFM material²⁵. In this work, we adopt bi-NiI₂ as the active antiferromagnet to demonstrate our above proposal. By combining bi-NiI₂ with FE In₂Se₃ with different thickness to design vdW heterostructure, the feasibility of realizing and controlling the half-metallicity in bi-NiI₂ by electric polarization flipping is investigated. It is found that the In₂Se₃ bilayer (bi-In₂Se₃) can successfully give rise to half-metallicity in bi-NiI₂. With the reversal of polarization from upward to downward for bi-In₂Se₃, the bi-NiI₂ undergoes a transformation from half-metal to semiconductor, accompanied by a switch of

¹State Key Lab of Crystal Materials and Institute of Crystal Materials, Shandong University, 250100 Jinan, China. ²Center for Optics Research and Engineering of Shandong University, Shandong University, 266237 Qingdao, China. ³Spintronics Institute, University of Jinan, 250022 Jinan, China. ✉email: sdy_liss@ujn.edu.cn; liyanlu@sdu.edu.cn

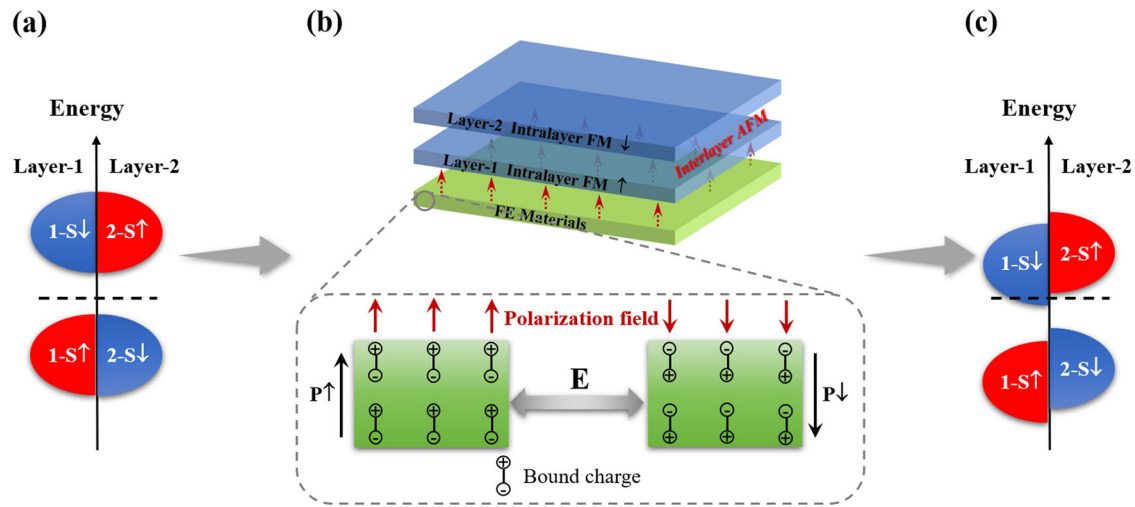


Fig. 1 Principle for realizing half-metallicity. **a** Schematic illustration of spin- and layer-projected DOS for a bilayer of A-type antiferromagnet. **b** Diagram of 2D A-type antiferromagnet on FE substrate. **c** Spin- and layer-projected DOS with half-metallicity.

easy magnetization axis from in-plane to out-of-plane direction. The nonvolatile electrical control of half-metallicity in bi-NiI₂ is the result of a combination of band shifts induced by the polarization field and selective charge transfer at the interface. Moreover, the strain is demonstrated as an additional route to modulate the half-metallic property and magnetic anisotropy energy (MAE). Two conceptual advanced nanodevices, a FE memory device, and a spin field effect transistor (SFET), are proposed based on the vdW heterostructure. These results provide an avenue to generate the switchable fully spin polarized current in AFM material, which would greatly promote the development of AFM spintronics.

RESULTS AND DISCUSSION

Physical properties of bi-NiI₂/In₂Se₃ heterostructure

We first explore the property of pristine bi-NiI₂. To evaluate the optimized structure, six stacking patterns were constructed for bi-NiI₂, shown in Supplementary Fig. 1a, in which the interlayer AFM and FM couplings were separately considered. The energy difference in Supplementary Table 1 reveals that the AB1 configuration with A-type AFM coupling is the most energetically stable. The optimized lattice constant and interlayer distance are 3.93 and 3.45 Å, respectively. We find that the spin moment is mainly contributed by the Ni atom, and the local magnetic moment of each Ni atom is about 2μ_B. Supplementary Fig. 1b presents the band structure of the bi-NiI₂, in which a semiconductor characteristic with an indirect bandgap of 1.27 eV can be observed. The conduction band minimum (CBM) and valence band maximum (VBM) are mainly dominated by the Ni-*d* and I-*p* orbitals, respectively. From the spin- and layer-projected DOS in Supplementary Fig. 1b, the spin subbands from the bottom NiI₂-1 layer and upper NiI₂-2 layer are strictly complemented, demonstrating the A-type AFM characteristic of the bi-NiI₂. A monolayer of In₂Se₃ was initially considered as the FE substrate due to its intrinsic out-of-plane FE nature. It shows a hexagonal structure with a lattice constant of 4.10 Å. The bistable polarized states are presented in Supplementary Fig. 2a, b, marked P↑ and P↓, which can be easily switched by a vertical electric field. The calculated band structure in Supplementary Fig. 2c demonstrates the semiconductor characteristic of the In₂Se₃ monolayer, accompanied by a bandgap of 0.78 eV. The VBM is mainly derived from the Se-*p* orbitals, while the CBM is jointly contributed by the In-*s* and the Se-*p* orbitals, which is consistent with the previous studies²⁶.

A small lattice mismatch of 4.1% between the bi-NiI₂ and the In₂Se₃ monolayer suggests a good quality vdW heterostructure

can be easily constructed, which is denoted as bi-NiI₂/In₂Se₃. Here, three stacking patterns were designed for two opposite polarized states, shown in Fig. 2a. Supplementary Table 2 lists the relative energies of different structures. It shows the DN-II and UP-II configurations, in which the Ni atom in the NiI₂-1 layer is located above the upper In atom of the adjacent In₂Se₃ monolayer, are energetically lower than the other configurations. More importantly, the A-type AFM coupling of bi-NiI₂ is maintained in the vdW heterostructure. The obtained interlayer distances between bi-NiI₂ and In₂Se₃ monolayer are 3.20 and 3.16 Å for P↑ and P↓ cases, respectively. This small difference implies that polarization switching has a negligible effect on the interlayer distance. Besides, the structural stability of vdW heterostructure was evaluated by the calculation of the formation energies, which is defined as $E_{\text{form}} = E(\text{bi-NiI}_2/\text{In}_2\text{Se}_3) - E(\text{bi-NiI}_2) - E(\text{In}_2\text{Se}_3)$, where the $E(\text{bi-NiI}_2/\text{In}_2\text{Se}_3)$, $E(\text{bi-NiI}_2)$, and $E(\text{In}_2\text{Se}_3)$ are total energies of bi-NiI₂/In₂Se₃ heterostructure, individual bi-NiI₂ and In₂Se₃ monolayer, respectively. The calculated formation energy is about -1.40 eV, suggesting the feasibility of experimental preparation of such vdW heterostructure. Based on the formation energy and interlayer distance, the interlayer vdW interaction in heterostructure is further demonstrated.

Then the electronic properties of bi-NiI₂/In₂Se₃ vdW heterostructures were investigated. Figure 2b, c present the calculated band structures and DOS of heterostructure. For the P↑ configuration, the band degeneracy of the bi-NiI₂ is removed due to different degrees of energy level shift for the NiI₂-1 and the NiI₂-2 layers, in which the spin splitting reaches up to about 73.4 meV. The heterostructure shows a semiconductor characteristic with an indirect bandgap of 476.6 meV. The CBM and VBM are dominated by the bi-NiI₂ and In₂Se₃ monolayer, respectively, indicating that the bi-NiI₂/In₂Se₃ belongs to a typical staggered-gap (type II) heterostructure. In the light of the orbital-projected band structure [see Supplementary Fig. 3a, b], the electronic states nearest to the E_F in conduction and valence bands are separately stemmed from the Ni-*d*_{yz}/*d*_{xz} and Se-*p*_x/*p*_y orbitals. Once the polarization is reversed to the P↓ case, the band structure of the heterostructure undergoes a dramatic change, shown in Fig. 2c. Although the type-II band alignment behavior is preserved, the domination components for the CBM and VBM are changed due to the relative displacement between the energy levels of the bi-NiI₂ and the In₂Se₃ monolayer. Under this circumstance, the conduction and valence band edges are originated from the In-*s*/Se-*p*_z and I-*p*_x/*p*_y orbitals, respectively [see Supplementary Fig. 3c, d]. In addition, the indirect bandgap of the heterostructure is

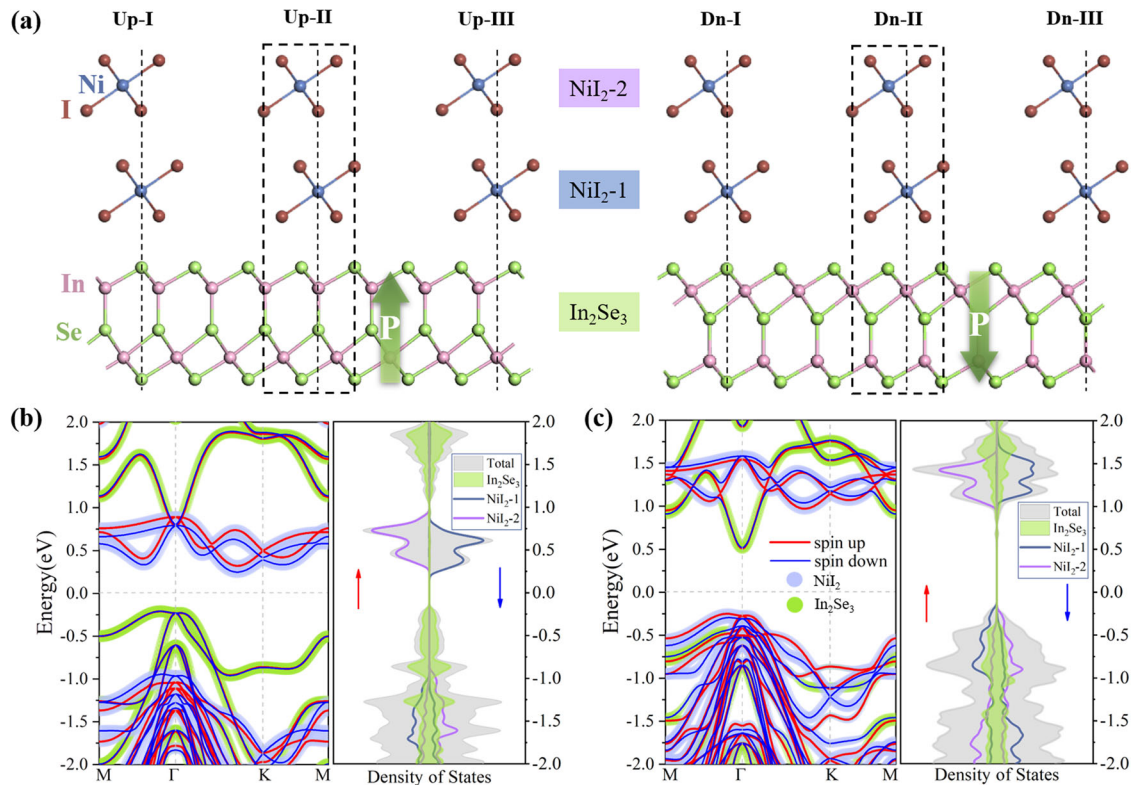


Fig. 2 Basic properties of bi-NiI₂/In₂Se₃ heterostructure. **a** Structural diagram of different stacking patterns for bi-NiI₂/In₂Se₃ heterostructure in the P_↑ and P_↓ configurations. **b, c** Calculated band structures and DOS of bi-NiI₂/In₂Se₃ heterostructure in the P_↑ and P_↓ configurations, respectively. The red and blue lines in the band structure represent spin-up and spin-down states, respectively.

increased to 802.4 meV, while the spin splitting of the bi-NiI₂ is reduced to about 51.5 meV. Generally, despite the spin splitting induced by the FE polarization, the energy bands contributed by the bi-NiI₂ and the In₂Se₃ monolayer in the vdW heterostructure are very similar to their pristine cases, which indicates that there is no obvious hybridization between the AFM bilayer and FE substrate.

The origin of the variation of band structure caused by the polarization flipping was also explored. The In₂Se₃ monolayer with out-of-plane FE polarization can produce an external polarization field. When the bi-NiI₂ is deposited on the In₂Se₃ monolayer, the polarization field would act upon the AFM bilayer. For the P_↑ case, the polarization field drives the energy levels of bi-NiI₂ to shift downward, which results in the CBM and VBM of bi-NiI₂ being lower than the CBM and VBM of In₂Se₃ monolayer [see Supplementary Fig. 4]. As a consequence, the CBM of the heterostructure is associated with the bi-NiI₂, while the VBM comes from the In₂Se₃ monolayer. It is important to point out that the distinct spatial position of NiI₂-1 and NiI₂-2 layers determines that their potential energies are different. As shown in Supplementary Fig. 5a, the potential energy difference between two NiI₂ layers turns out to be 0.24 eV, and thus two NiI₂ layers exhibit unequal energy level shift, which gives rise to the band spin splitting. However, for the heterostructure in the P_↓ configuration, the energy bands of bi-NiI₂ shift to higher energy since the polarization field is reversed. This shift of energy level finally leads to the CBM dominated by the In₂Se₃ monolayer and the VBM dominated by the bi-NiI₂ [see Supplementary Fig. 4], in contrast with the P_↑ case. Furthermore, the potential energy difference between two NiI₂ layer is decreased to 0.16 eV in this situation, shown in Supplementary Fig. 5b, which contributes to a smaller spin splitting for the bi-NiI₂. In a word, although the In₂Se₃ monolayer would not bring about qualitative change for the electronic property of bi-NiI₂, the generated electric polarization

indeed drives the downward shift of energy level of bi-NiI₂, which offers an opportunity to further manipulate the electronic property by enhancing polarization field.

Physical properties of bi-NiI₂/bi-In₂Se₃ heterostructure

To verify the above conception, one more In₂Se₃ layer was added at the bottom of bi-NiI₂/In₂Se₃. This vdW heterostructure is named bi-NiI₂/bi-In₂Se₃. Here, for simplicity, two different polar configurations were taken into account for the bi-In₂Se₃, i.e., the polarization directions of FE layers were both pointing upward (P_{↑↑}) or downward (P_{↓↓}). The stacking pattern of the bi-In₂Se₃ was also optimized and shown in Supplementary Fig. 2d. It reveals that in the most stable configuration, the upper In atom in the In₂Se₃-1 layer is vertically aligned with the upper Se atom in the In₂Se₃-2 layer. Figure 3a, b show the geometric structures of bi-NiI₂/bi-In₂Se₃ in the P_{↑↑} and P_{↓↓} configurations. The calculated formation energy of the bi-NiI₂/bi-In₂Se₃ is about -0.09 eV, suggesting that such a complex heterostructure is promising to be produced. The interlayer distance at the NiI₂-In₂Se₃ interface is insensitive to the addition of the second In₂Se₃ layer, and it is found to be 3.20 and 3.19 Å for the P_{↑↑} and P_{↓↓} cases, respectively. Remarkably, the A-type AFM ground state of the bi-NiI₂ is persisted, which is immune to the polarization direction of the substrate, and the energy differences between AFM and FM states for the P_{↑↑} and P_{↓↓} cases are 9.68 and 10.68 meV per unit cell, respectively.

The effect of the bi-In₂Se₃ on the electronic property of the bi-NiI₂ was also investigated. The layer- and spin-projected band structures and DOS of bi-NiI₂/bi-In₂Se₃ heterostructures are plotted in Fig. 3c, d. For the P_{↑↑} configuration, the spin splitting of the energy band for the bi-NiI₂ is increased to 138.7 meV because of the enhanced polarization field from the FE substrate, which is about double that of bi-NiI₂/In₂Se₃. More interestingly, the E_F passes through the spin-down conduction band edge,

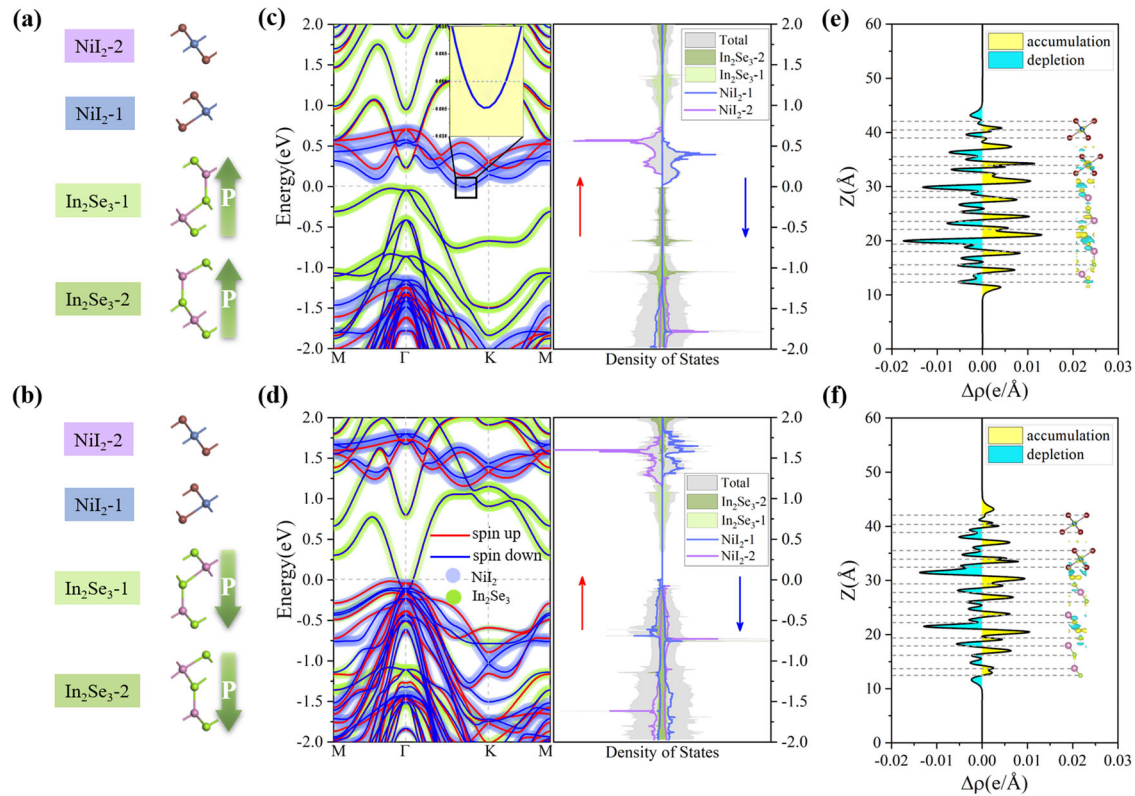


Fig. 3 Basic properties of bi-NiI₂/bi-In₂Se₃ heterostructure. **a, b** Structural diagrams, **c, d** calculated band structures and DOSs, and **e, f** differential charge distributions of bi-NiI₂/bi-In₂Se₃ heterostructure in the P↑ and P↓ configurations, respectively. The red and blue lines in band structures represent spin-up and spin-down states, respectively.

which forms an interesting band structure with half-metallicity, shown in Fig. 3c. From the DOS analysis, the electronic states at the E_F are contributed by the NiI₂-1 layer, while the NiI₂-2 layer remains the semiconducting property. To be brief, the bi-NiI₂ possesses the AFM half-metallicity under the action of the upward FE polarization from the substrate, which makes the generation of fully polarized current possible. By flipping the electric polarization of bi-In₂Se₃, we find that the energy bands associated with the bi-NiI₂ shift upward relative to the E_F , and the intersection between them is vanished, implying that the bi-NiI₂ restores the semiconducting nature, as depicted in Fig. 3d. Meanwhile, the spin splitting is decreased to 98.9 meV. However, for the heterostructure, it exhibits a metallic characteristic since the E_F cuts through the energy band contributed by the bi-In₂Se₃. Despite the presence of the conductive state for both P↑ and P↓ cases, the produced currents in heterostructure are distinctly different: the former is fully spin polarized and localized in the bi-NiI₂, while the latter is spin depolarized and existed in the bi-In₂Se₃ substrate.

Next, we discuss the underlying physics for the electrically controlled half-metallicity in the AFM bi-NiI₂. With the increase of the thickness of FE layer, the generated polarization field is enhanced correspondingly, which further improves the degrees of band shift and spin-splitting of bi-NiI₂. For the P↑ case, the enhanced polarization field offers a prerequisite to realizing the half-metallicity for bi-NiI₂, while the charge transfer at the NiI₂-In₂Se₃ interface plays a decisive role. Figure 3e, f present the three-dimensional (3D) and plane-integrated differential charge distribution of bi-NiI₂/bi-In₂Se₃. It can be seen that the charge transfer is mainly located at the NiI₂-In₂Se₃ and the In₂Se₃-In₂Se₃ interfaces, whereas it is almost negligible between the NiI₂-1 and the NiI₂-2 layers. This can be explained by comparing the work functions of the In₂Se₃ and the NiI₂ pristine layers. Since the In₂Se₃

layer is highly polarized, the calculated work functions on the two sides of the sample are different, i.e., $W_1 = 5.24$ eV for the Se₊ surface and $W_2 = 6.03$ eV for the Se₋ surface. However, for the nonpolar NiI₂ monolayer, the work function shows a single value of $W = 5.62$ eV. Hence, the obtained work functions satisfy the relationship of $W_1 < W < W_2$. With an upward polarization direction, the electrons would transfer from the In₂Se₃-1 to the NiI₂-1, shown in Fig. 3e. The charge transfer will result in the electrons depletion at the upper surface of In₂Se₃-1 and the electron accumulation at the lower surface of NiI₂-1, respectively. The extra electrons in the NiI₂-1 layer will partially occupy the conduction band edge, leading to the phenomenon of electron doping. Therefore, the half-metallicity in the bi-NiI₂ is the synergistic result of the polarization field induced variation of band alignment and charge redistribution induced electron doping. With the reversal of the electric polarization, the electrons in the NiI₂-1 layer tend to transfer to the In₂Se₃-2 layer due to $W < W_2$ [see Fig. 3f], which endows the bi-In₂Se₃ substrate with electron doping and conductive state. On the other hand, the work function at the In₂Se₃-In₂Se₃ interface is invariably different, and thus the charge transfer associated with the polarization direction is inevitable. The inappreciable interlayer charge transfer between the NiI₂ layers can be attributed to the identical work function between the two layers.

For the AFM materials, the manipulation of easy magnetization axis is of significance and has attracted great attention^{27–32}. Thus it is important to identify the response of the easy magnetization axis of bi-NiI₂ to the polarization switching. Then the MAE of the bi-NiI₂/bi-In₂Se₃ heterostructure was calculated. The result indicates that the MAE of the bi-NiI₂ is isotropic within the xy plane, regardless of the polarization direction of the FE substrate. Figure 4a, b show the MAE associated with polar angle θ . It is observed that the easy magnetization axis for the P↑ and P↓ cases are in-

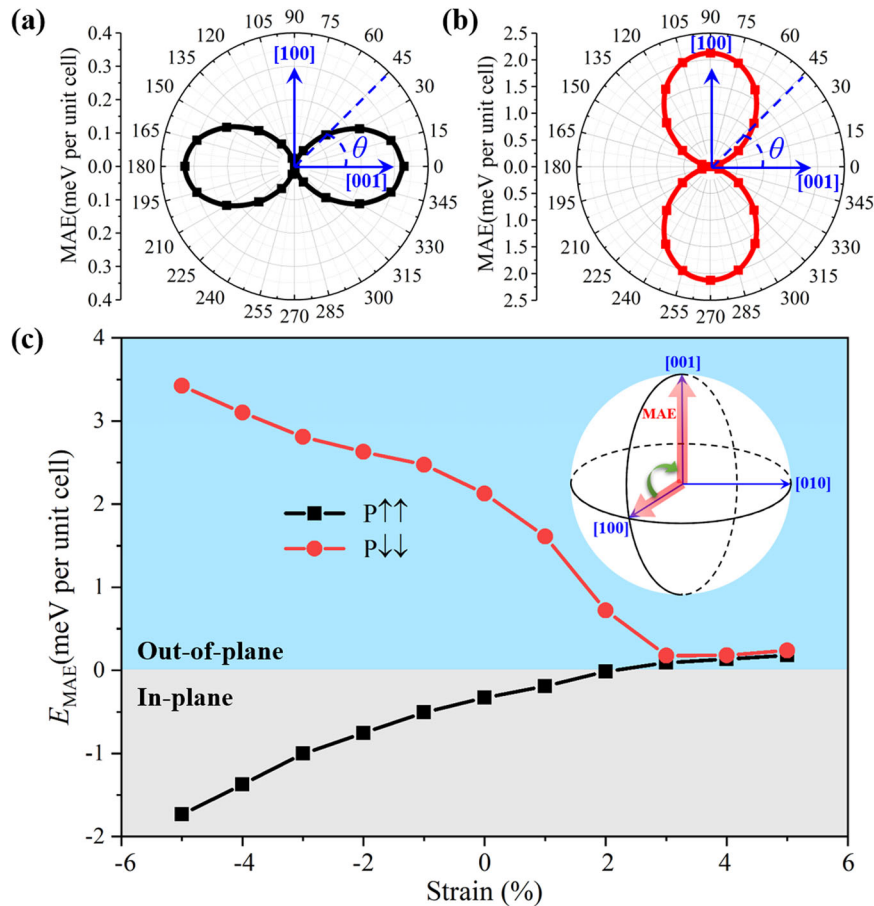


Fig. 4 MAE of bi-NiI₂/bi-In₂Se₃ heterostructure. **a, b** Polar angle θ dependence of MAE with a - c plane for $P\uparrow\uparrow$ and $P\downarrow\downarrow$ cases, respectively. **c** Variation of E_{MAE} as a function of biaxial strain for $P\uparrow\uparrow$ and $P\downarrow\downarrow$ cases.

plane and out-of-plane, respectively. Hence, the polarization flipping of substrate can effectively switch the easy magnetization axis of the bi-NiI₂. The magnitude of MAE for the bi-NiI₂/bi-In₂Se₃ is considerably larger than those of Sc₂CO₂/VSe₂ and bi-CrI₃/Sc₂CO₂ heterostructures^{33,34}. From the layer-resolved MAE in Supplementary Fig. 6a, one can see that the MAE of heterostructures is mainly contributed by the I atoms in the bi-NiI₂, while the contribution of the bi-In₂Se₃ can be almost ignored. With regard to the I atom, the hybridization between p_x and p_y orbitals as well as the hybridization between p_y and p_z orbitals jointly constitute the MAE, in which the former and the latter are responsible for the in-plane and the out-of-plane magnetic anisotropy, respectively, as illustrated in Supplementary Fig. 6b, c. The reversal of easy magnetization axis in the bi-NiI₂ triggered by the polarization switching of the substrate can be understood by the competition between these two hybridizations. When the electric polarization of bi-In₂Se₃ is upward (downward), the p_x and p_y (p_y and p_z) hybridization is stronger than the p_y and p_z (p_x and p_y) hybridization, which leads to the in-plane (out-of-plane) magnetic anisotropy [see Supplementary Fig. 6b, c]. Moreover, we notice that the bi-NiI₂ shows an easy-plane magnetization when the substrate is in the $P\uparrow\uparrow$ configuration. Very recently, the antiferromagnetism and the magnetic transition temperature have been demonstrated experimentally in the bi-CrCl₃ which also has an easy magnetization plane^{35,36}. Therefore, the long-range AFM order and half-metallicity in bi-NiI₂ are expected to be existent at finite temperature. With these outstanding advantages, the bi-NiI₂/bi-In₂Se₃ heterostructure shows promising potential for the application as an efficient nonvolatile memory.

Effect of strain on bi-NiI₂/bi-In₂Se₃ heterostructure

As mentioned above, the upward FE polarization can induce the electron doping for bi-NiI₂, while the downward FE polarization drives the valence band edge of the bi-NiI₂ extremely close to the E_F . Such electronic properties suggest that external means, such as in-plane biaxial strain, may further tailor the electronic behavior of the heterostructure. Supplementary Fig. 7 shows the band structures of heterostructure under different biaxial strains. When the compressive strain is applied, the energy band dispersion becomes more extended because of bond length shortening. For the heterostructure in the $P\uparrow\uparrow$ configuration, this would enhance the electron doping in the bi-NiI₂, which in turn increases the conductivity of the half-metallic bi-NiI₂. Meanwhile, for the $P\downarrow\downarrow$ case, the valence band edge of the bi-NiI₂ shifts upward continuously with the increase of the compressive strain, and finally intersects with the E_F at -3% of strain, leading to a hole doping induced half-metallicity. Such half-metallicity is also stemmed from the NiI₂-1 layer, but determined by the spin-up state. Thus, within an appropriate range of the compressive strain, the half-metallicity of the bi-NiI₂ becomes independent of polarization flipping, whereas the reversal of the polarization can effectively switch the type of charge carrier and the spin orientation of the fully spin polarized current. On the contrary, the tensile strain would enlarge the bond length and improve the localization of energy bands. Once the tensile strain is implemented, the bi-NiI₂ would restore the semiconducting property due to the depletion of the doped electrons [see Supplementary Fig. 7c]. Hence, for developing spintronics applications, the manipulation with compressive strain is more effective for providing better spin control. The effect of biaxial strain on the

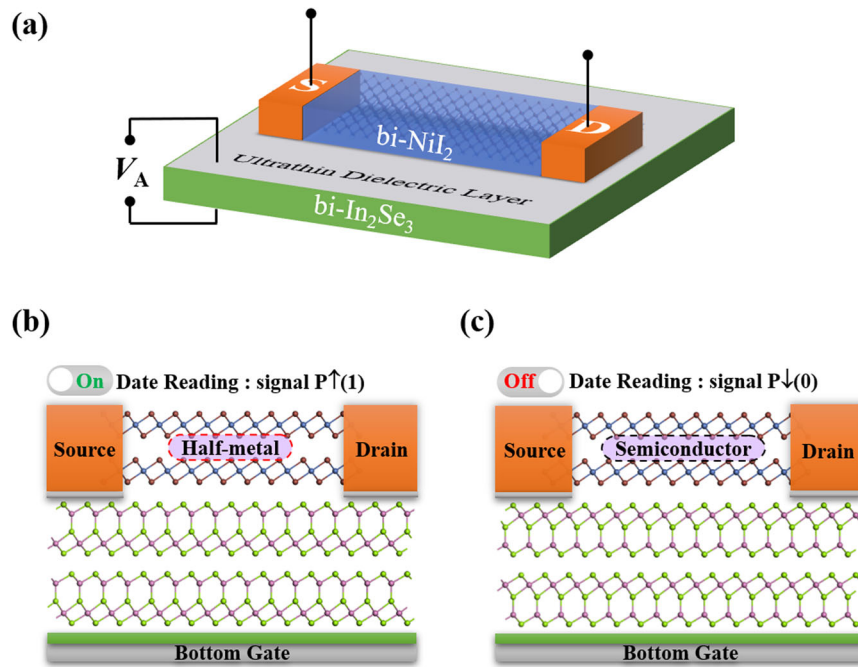


Fig. 5 Device prototype and schematic diagram. **a** Prototypes of the ferroelectric memory device and spin-field effect transistor based on the $\text{bi-NiI}_2/\text{bi-In}_2\text{Se}_3$ heterostructure. **b, c** Operation principle of ferroelectric memory device whose data writing depends on FE $\text{bi-In}_2\text{Se}_3$ and data reading is based on the different electric signal.

MAE was also studied. The energy difference between the magnetization in x (100) and z (001) directions was calculated, which is defined as $E_{\text{MAE}} = E_{100} - E_{001}$. The evolution of E_{MAE} as a function of biaxial strain is displayed in Fig. 4c. For the $\text{P}\uparrow\uparrow$ case, the E_{MAE} is diminished gradually in the strain range of -5% to 2% . To figure out the mechanism of the MAE change, we further analyze the orbital-resolved MAE of the I atom in the heterostructure under different strain, as depicted in Supplementary Fig. 8. The result reveals that the MAE contribution from the p_x and p_y hybridization is decreased significantly in the strain range from -5% to 2% , while the p_y and p_z hybridization is almost unchanged, which results in the decrease of E_{MAE} . More interestingly, the E_{MAE} becomes positive and increases slightly when the tensile strain is larger than 3% , indicating that the easy magnetization axis is switched from in-plane to out-of-plane. This is due to the fact that the continuous decrease of the hybridization between p_x and p_y orbitals makes the p_y and p_z hybridization dominate the MAE. It is worth mentioning that the E_{MAE} at the 3% tensile strain is $91 \mu\text{eV}$ per unit cell ($45.5 \mu\text{eV}$ per Ni atom), comparable to those of monolayers CrSnTe_3 ($69 \mu\text{eV}$ per Cr atom) and VSi_2N_4 ($64 \mu\text{eV}$ per V atom)^{37,38}, suggesting that the heterostructure still holds the potential for magnetoelectronic applications. On the other hand, for the $\text{P}\downarrow\downarrow$ case, the E_{MAE} also shows a decrease trend in the strain range from -5% to 3% . It is caused by the significant enhancement of the p_x and p_y hybridization and the slight decrease of the p_y and p_z hybridization [see Supplementary Fig. 9], which is distinct from that of the heterostructure in the $\text{P}\uparrow\uparrow$ configuration. Besides, as the tensile strain is larger than 3% , the E_{MAE} tends to remain constant. To understand this phenomenon, the layer-resolved MAE under the tensile strain is plotted in Supplementary Fig. 10. It shows that the MAE is jointly determined by the I and Ni atoms, in which the former and the latter contribute to the out-of-plane and in-plane magnetic anisotropy, respectively. The overall contributions from the I atoms are enhanced with increasing tensile strain, while the same trend is obtained for the Ni atom. Therefore, the E_{MAE} is hardly changed in this scenario.

FE memory device based on $\text{bi-NiI}_2/\text{bi-In}_2\text{Se}_3$

The results have demonstrated that the heterostructure possesses the capacity of controlling the half-metallicity by FE polarization, which provides a promising opportunity for designing FE memory devices. Here, a prototype of a memory device is proposed based on the heterostructure, shown in Fig. 5a. The electric polarization in the $\text{bi-In}_2\text{Se}_3$ is switched by an independent voltage V_A , and the bi-NiI_2 as the conducting channel is contacted with the source/drain. When the FE substrate is in the $\text{P}\uparrow\uparrow$ configuration, the electron would travel through the channel layer with 100% spin polarization, due to the half-metallicity of the bi-NiI_2 . Such conductive state is denoted “1” or “ON” state of the device, shown in Fig. 5b. By flipping the FE substrate to the $\text{P}\downarrow\downarrow$ configuration, the bi-NiI_2 becomes a semiconductor and the traveling of electrons is forbidden. This corresponds to the “0” or “OFF” state of the device, shown in Fig. 5c. In this context, the data reading process is accessible by converting the FE polarization state of $\text{bi-In}_2\text{Se}_3$ into conducting state of bi-NiI_2 and detecting it, which can effectively avoid the destructive effect caused by detecting the polarized state. Furthermore, the scheme in Fig. 5a can also be adopted into SFETs. Different from a traditional semiconductor transistor with modulating the charge populations, the working principle of $\text{bi-NiI}_2/\text{bi-In}_2\text{Se}_3$ heterostructure based SFET is manipulating the band structure of the AFM bilayer via controlling the FE polarization of the substrate. As a result, this SFET not only has the advantage of rapid response but more importantly, the regulation between different states is nonvolatile. Therefore, the SFET can be used in high-performance and low-power consumption devices.

To realize the above device functions, switching the polarization of the FE substrate via external electric field is a very vital task. However, the result has revealed that the FE $\text{bi-In}_2\text{Se}_3$ is conductive in the heterostructure when the electric polarization is downward. For a metallic FE material, the polarization is difficult to be switched since the required voltage bias will produce a high electrical current rather than changing the structural polarity. Inspired by the recently successful case of the polarization reversal in the FE semimetal WTe_2 ³⁹, it is possible to eliminate the electrical

current by inserting a dielectric layer into the bi-NiI₂/bi-In₂Se₃ heterostructure, which might be able to achieve the polarization switching via an external electric field. In addition, the FE bistability of bi-NiI₂/bi-In₂Se₃ was also investigated, since it is closely associated with device performance. As a matter of fact, the polarization reversal in the FE In₂Se₃ layer requires undergoing an intermediate antiferroelectric (AFE) state. Thus the heterostructure in the AFE configuration was constructed, shown in Supplementary Fig. 11. By calculating the total energy, we find that the total energy of the AFE configuration is 2.05 eV per unit cell, higher than the P↑↑ and P↓↓ cases. Therefore, the bi-NiI₂/bi-In₂Se₃ heterostructure offers sufficient bistability for the device application.

Physical properties of bi-NiI₂/tri-In₂Se₃ heterostructure

From the above results, we extract that the electronic property of the bi-NiI₂ shows different response to the In₂Se₃ layer with different thickness. To clarify the thickness effect of the In₂Se₃, on the basis of bi-NiI₂/bi-In₂Se₃, we further added one more In₂Se₃ layer to construct the bi-NiI₂/tri-In₂Se₃ heterostructure. After structural optimization, the most stable geometric structures of bi-NiI₂/tri-In₂Se₃ with two opposite polarized configurations are displayed in Supplementary Fig. 12a, b. The formation energy of the heterostructure is evaluated to be about -0.01 meV, and the interlayer distances between the bi-NiI₂ and the tri-In₂Se₃ are 3.24 and 3.22 Å for the P↑↑↑ and P↓↓↓ cases, respectively. By comparing the energy between different magnetic configurations, as listed in Supplementary Table 3, we find that the bi-NiI₂ still maintains the A-type AFM coupling in the heterostructure. Supplementary Fig. 12c, d present the calculated band structures of heterostructures. Different from the bi-NiI₂/bi-In₂Se₃, the bi-NiI₂/tri-In₂Se₃ in the P↑↑↑ configuration in general shows a metallic property, which is featured with the intersection between E_F and energy bands originated from both bi-NiI₂ and tri-In₂Se₃. Fortunately, the bi-NiI₂ still harbors the AFM half-metallicity in this situation, and the fully spin polarized (spin-down) state is come from the NiI₂-1 layer, as illustrated in Supplementary Fig. 12c. The effect of the increase of In₂Se₃ layer is mainly manifested in two aspects: the spin splitting of NiI₂ is enhanced to 151.97 meV; the FE substrate becomes metallic. On the other hand, when the electric polarization of the FE substrate is downward, the bi-NiI₂/tri-In₂Se₃ possesses a similar electronic characteristic to that of bi-NiI₂/bi-In₂Se₃. However, there is a significant difference between them. The bi-NiI₂ in the bi-NiI₂/tri-In₂Se₃ is also endowed with the half-metallicity since the E_F passes through the spin-up state arisen from the NiI₂-1 layer, which is distinct from the semiconducting nature in the bi-NiI₂/bi-In₂Se₃. The emergence of such half-metallicity is result from the hole doping in the bi-NiI₂. With the increase of In₂Se₃ layer, the electron transfer from NiI₂-1 to In₂Se₃-1 is enhanced correspondingly. Combined with the upward shift of energy level of the bi-NiI₂ induce by the polarization field, the sufficient electron transfer can give rise to the hole doping for the valence band edge, and thus half-metallic property is produced in the bi-NiI₂. Besides, the spin splitting of the bi-NiI₂ is reduced to 80.72 meV. In brief, when the tri-In₂Se₃ is employed as the substrate, the bi-NiI₂ always shows the AFM half-metallicity, with the fully spin-polarized state being localized at the NiI₂-1 layer, while the heterostructure exhibits a metallic band structure. The reversal of electric polarization of the tri-In₂Se₃ can effectively flip the spin polarity of the half-metallic bi-NiI₂.

In summary, we have proposed vdW heterostructures formed by A-type AFM bi-NiI₂ and FE In₂Se₃ with different thickness. With first-principles calculations, the switchable half-metallicity is realized in the bi-NiI₂/bi-In₂Se₃ heterostructure. The polarization flipping of bi-In₂Se₃ from upward to downward would convert the bi-NiI₂ from half-metal to semiconductor. Meanwhile, the easy

magnetization axis of bi-NiI₂ also undergoes a transition from the in-plane to the out-of-plane direction. It shows that the cooperation between the band shift induced by the polarization field and selective charge transfer at the interface is responsible for achieving the nonvolatile half-metallicity. The half-metallic behavior and the MAE in the heterostructure can be further adjusted by introducing strain. The prototypes of a FE memory device and SFET are designed using the vdW heterostructure. This work offers a possible scheme to achieve and control the half-metallicity in 2D A-type antiferromagnet. It opens opportunities for spintronic devices.

METHODS

First principles calculations were performed within the framework of density functional theory (DFT) by the projector-augmented wave (PAW) method⁴⁰, as implemented in the Vienna ab initio simulation package (VASP)^{41,42}. The Perdew–Burke–Ernzerhof generalized gradient approximation (GGA) was adopted to describe the exchange and correlation functional^{43,44}. The kinetic energy cutoff of 500 eV for the plane-wave basis set was used throughout the calculation. Structural relaxations were carried out until the residual force on each atom was <0.005 eV/Å, and the energy convergence criteria of 10⁻⁶ eV was employed. The Brillouin zone was sampled using a Γ -centered Monkhorst–Pack scheme with 17 × 17 × 1. A vacuum layer with a thickness larger than 30 Å was set to eliminate interactions between periodic images. The interlayer vdW interaction is described by the DFT-D3 method^{45,46}. The GGA + U method was employed to treat the strongly correlated Ni-3d electrons⁴⁷. To determine the appropriate effective Hubbard U (U_{eff}) for the bi-NiI₂, the band structures with U_{eff} varying from 0.0 to 8.0 eV were calculated, as illustrated in Supplementary Fig. 13. By comparing the bandgap obtained from the GGA + U method with that from the experiment²⁵, we found that the result of $U_{\text{eff}} = 5.0$ eV is more reliable, and thus the $U_{\text{eff}} = 5.0$ eV was adopted in our calculation.

DATA AVAILABILITY

The authors declare that the main data supporting the findings of this study are available within the article and its Supplementary Information files.

CODE AVAILABILITY

The central codes used in this paper are VASP. Detailed information related to the license and user guide are available at <https://www.vasp.at>.

Received: 20 May 2022; Accepted: 11 October 2022;
Published online: 23 October 2022

REFERENCES

- Jungwirth, T., Marti, X., Wadley, P. & Wunderlich, J. Antiferromagnetic spintronics. *Nat. Nanotechnol.* **11**, 231–241 (2016).
- Jungwirth, T. et al. The multiple directions of antiferromagnetic spintronics. *Nat. Phys.* **14**, 200–203 (2018).
- Baltz, V. et al. Antiferromagnetic spintronics. *Rev. Mod. Phys.* **90**, 015005 (2018).
- Železný, J., Wadley, P., Olejník, K., Hoffmann, A. & Ohno, H. Spin transport and spin torque in antiferromagnetic devices. *Nat. Phys.* **14**, 220–228 (2018).
- Baldrati, L. et al. Mechanism of Néel order switching in antiferromagnetic thin films revealed by magnetotransport and direct imaging. *Phys. Rev. Lett.* **123**, 177201 (2019).
- Holzberger, S., Schuh, T., Blügel, S., Lounis, S. & Wulffhkel, W. Parity effect in the ground state localization of antiferromagnetic chains coupled to a ferromagnet. *Phys. Rev. Lett.* **110**, 157206 (2013).
- Xu, Y., Wang, S. & Xia, K. Spin-transfer torques in antiferromagnetic metals from first principles. *Phys. Rev. Lett.* **100**, 226602 (2008).
- Hu, X. Half-metallic antiferromagnet as a prospective material for spintronics. *Adv. Mater.* **24**, 294–298 (2012).

9. Tong, J. et al. High and reversible spin polarization in a collinear antiferromagnet. *Appl. Phys. Rev.* **7**, 031405 (2020).
10. Wadley, P. et al. Electrical switching of an antiferromagnet. *Science* **351**, 587–590 (2016).
11. Gong, S. J. et al. Electrically induced 2D half-metallic antiferromagnets and spin field effect transistors. *Proc. Natl Acad. Sci. USA* **115**, 8511–8516 (2018).
12. Geim, A. K. & Grigorieva, I. V. Van der Waals heterostructures. *Nature* **499**, 419–425 (2013).
13. Gong, C. & Zhang, X. Two-dimensional magnetic crystals and emergent heterostructure devices. *Science* **363**, eaav4450 (2019).
14. Novoselov, K. S., Mishchenko, A., Carvalho, A. & Castro Neto, A. H. 2D materials and van der Waals heterostructures. *Science* **353**, aac9439 (2016).
15. Gong, C., Kim, E. M., Wang, Y., Lee, G. & Zhang, X. Multiferroicity in atomic van der Waals heterostructures. *Nat. Commun.* **10**, 2657 (2019).
16. Li, Z. & Zhou, B. Theoretical investigation of nonvolatile electrical control behavior by ferroelectric polarization switching in two-dimensional $\text{MnCl}_2/\text{CuInP}_2\text{S}_6$ van der Waals heterostructures. *J. Mater. Chem. C* **8**, 4534–4541 (2020).
17. Liu, W.-R. et al. Magnetic anisotropy and ferroelectric-driven magnetic phase transition in monolayer $\text{Cr}_2\text{Ge}_2\text{Te}_6$. *Nanoscale* **14**, 3632–3643 (2022).
18. Pei, Q., Zhou, B., Mi, W. & Cheng, Y. Triferroic material and electrical control of valley degree of freedom. *ACS Appl. Mater. Interfaces* **11**, 12675–12682 (2019).
19. Zhao, Y., Zhang, J. J., Yuan, S. & Chen, Z. Nonvolatile electrical control and heterointerface-induced half-metallicity of 2D ferromagnets. *Adv. Funct. Mater.* **29**, 1901420 (2019).
20. Sun, W., Wang, W., Chen, D., Cheng, Z. & Wang, Y. Valence mediated tunable magnetism and electronic properties by ferroelectric polarization switching in 2D $\text{Fe}_2/\text{In}_2\text{Se}_3$ van der Waals heterostructures. *Nanoscale* **11**, 9931–9936 (2019).
21. Bonilla, M. et al. Strong room-temperature ferromagnetism in VSe_2 monolayers on van der Waals substrates. *Nat. Nanotechnol.* **13**, 289–293 (2018).
22. Fei, Z. et al. Two-dimensional itinerant ferromagnetism in atomically thin Fe_3GeTe_2 . *Nat. Mater.* **17**, 778–782 (2018).
23. Gong, C. et al. Discovery of intrinsic ferromagnetism in two-dimensional van der Waals crystals. *Nature* **546**, 265–269 (2017).
24. Huang, B. et al. Layer-dependent ferromagnetism in a van der Waals crystal down to the monolayer limit. *Nature* **546**, 270–273 (2017).
25. Liu, H. et al. Vapor deposition of magnetic van der Waals Ni_2 crystals. *ACS Nano* **14**, 10544–10551 (2020).
26. Tian, H. et al. Band structure engineering of van der Waals heterostructures using ferroelectric clamped sandwich structures. *Phys. Rev. B* **103**, 125426 (2021).
27. Fukami, S., Zhang, C., DuttaGupta, S., Kurenkov, A. & Ohno, H. Magnetization switching by spin-orbit torque in an antiferromagnet-ferromagnet bilayer system. *Nat. Mater.* **15**, 535–541 (2016).
28. Kurenkov, A., Zhang, C., DuttaGupta, S., Fukami, S. & Ohno, H. Device-size dependence of field-free spin-orbit torque induced magnetization switching in antiferromagnet/ferromagnet structures. *Appl. Phys. Lett.* **110**, 092410 (2017).
29. Oh, Y.-W. et al. Field-free switching of perpendicular magnetization through spin-orbit torque in antiferromagnet/ferromagnet/oxide structures. *Nat. Nanotechnol.* **11**, 878–884 (2016).
30. Peng, S. et al. Exchange bias switching in an antiferromagnet/ferromagnet bilayer driven by spin-orbit torque. *Nat. Electron.* **3**, 757–764 (2020).
31. Wang, Y. et al. Magnetization switching by magnon-mediated spin torque through an antiferromagnetic insulator. *Science* **366**, 1125–1128 (2019).
32. Zhang, P. X. et al. Spin-orbit torque in a completely compensated synthetic antiferromagnet. *Phys. Rev. B* **97**, 214403 (2018).
33. Lu, Y. et al. Artificial multiferroics and enhanced magnetoelectric effect in van der Waals heterostructures. *ACS Appl. Mater. Interfaces* **12**, 6243–6249 (2020).
34. Jiang, P. et al. Ferroelectric control of electron half-metallicity in A-type antiferromagnets and its application to nonvolatile memory devices. *Phys. Rev. B* **102**, 245417 (2020).
35. Cai, X. et al. Atomically thin CrCl_3 : an in-plane layered antiferromagnetic insulator. *Nano Lett.* **19**, 3993–3998 (2019).
36. Kim, H. H. et al. Evolution of interlayer and intralayer magnetism in three atomically thin chromium trihalides. *Proc. Natl Acad. Sci. USA* **116**, 11131–11136 (2019).
37. Cui, Q., Zhu, Y., Liang, J., Cui, P. & Yang, H. Spin-valley coupling in a two-dimensional VSi_2N_4 monolayer. *Phys. Rev. B* **103**, 085421 (2021).
38. Zhuang, H. L., Xie, Y., Kent, P. R. C. & Ganesh, P. Computational discovery of ferromagnetic semiconducting single-layer CrSnTe_3 . *Phys. Rev. B* **92**, 035407 (2015).
39. Sharma, P. et al. A room-temperature ferroelectric semimetal. *Sci. Adv.* **5**, eaax5080 (2019).
40. Kresse, G. & Joubert, D. From ultrasoft pseudopotentials to the projector augmented-wave method. *Phys. Rev. B* **59**, 1758–1775 (1999).
41. Kresse, G. & Furthmüller, J. Efficient iterative schemes for ab initio total-energy calculations using a plane-wave basis set. *Phys. Rev. B* **54**, 11169–11186 (1996).
42. Kresse, G. & Hafner, J. Ab initio molecular-dynamics simulation of the liquid-metal-amorphous-semiconductor transition in germanium. *Phys. Rev. B* **49**, 14251–14269 (1994).
43. Grimme, S. Semiempirical GGA-type density functional constructed with a long-range dispersion correction. *J. Comput. Chem.* **27**, 1787–1799 (2006).
44. Perdew, J. P. & Wang, Y. Accurate and simple analytic representation of the electron-gas correlation energy. *Phys. Rev. B* **45**, 13244–13249 (1992).
45. Grimme, S., Antony, J., Ehrlich, S. & Krieg, H. A consistent and accurate ab initio parametrization of density functional dispersion correction (DFT-D) for the 94 elements H-Pu. *J. Chem. Phys.* **132**, 154104 (2010).
46. Grimme, S., Ehrlich, S. & Goerigk, L. Effect of the damping function in dispersion corrected density functional theory. *J. Comput. Chem.* **32**, 1456–1465 (2011).
47. Dudarev, S. L., Botton, G. A., Savrasov, S. Y., Humphreys, C. J. & Sutton, A. P. Electron-energy-loss spectra and the structural stability of nickel oxide: an LSDA +U study. *Phys. Rev. B* **57**, 1505–1509 (1998).

ACKNOWLEDGEMENTS

This work was supported by the National Natural Science Foundation of China (Grant Nos. 12004137 and 11974145), the Key Research and Development Program of Shandong Province (No. 2019JZZY010313), and Natural Science Foundation of Shandong Province (Grant Nos. ZR2020QA052 and ZR2020ZD28).

AUTHOR CONTRIBUTIONS

S.L. conceived the idea and designed the project, Y.W. performed the calculations and wrote the paper with the help of S.L. and W.J., Q.C. participated in the discussion and writing of device applications. X.X., X.Z., and Y.L. supervised the project. All authors analyzed the data and contributed to the discussions of the results.

COMPETING INTERESTS

The authors declare no competing interests.

ADDITIONAL INFORMATION

Supplementary information The online version contains supplementary material available at <https://doi.org/10.1038/s41524-022-00904-6>.

Correspondence and requests for materials should be addressed to Shengshi Li or Yanlu Li.

Reprints and permission information is available at <http://www.nature.com/reprints>

Publisher's note Springer Nature remains neutral with regard to jurisdictional claims in published maps and institutional affiliations.



Open Access This article is licensed under a Creative Commons Attribution 4.0 International License, which permits use, sharing, adaptation, distribution and reproduction in any medium or format, as long as you give appropriate credit to the original author(s) and the source, provide a link to the Creative Commons license, and indicate if changes were made. The images or other third party material in this article are included in the article's Creative Commons license, unless indicated otherwise in a credit line to the material. If material is not included in the article's Creative Commons license and your intended use is not permitted by statutory regulation or exceeds the permitted use, you will need to obtain permission directly from the copyright holder. To view a copy of this license, visit <http://creativecommons.org/licenses/by/4.0/>.

© The Author(s) 2022